geosciences

MDPI

Article

Hydroacoustic Monitoring of Mayotte Submarine Volcano during Its Eruptive Phase

Aude Lavayssière *, Sara Bazin and Jean-Yves Royer

Geo-Ocean, Univ Brest, CNRS, IFREMER, UMR6538, IUEM, F-29280 Plouzane, France
* Correspondence: aude.lavayssiere@gmail.com

Abstract: Submarine volcanoes are more challenging to monitor than subaerial volcanoes. Yet, the large eruption of the Hunga Tonga-Hunga Ha'apai volcano in the Tonga archipelago in 2022 was a reminder of their hazardous nature and hence demonstrated the need to study them. In October 2020, four autonomous hydrophones were moored in the sound fixing and ranging channel 50 km offshore Mayotte Island, in the North Mozambique Channel, to monitor the Fani Maoré 2018–2020 submarine eruption. Between their deployment and July 2022, this network of hydrophones, named MAHY, recorded sounds generated by the recent volcanic activity, along with earthquakes, submarine landslides, marine mammals calls, and marine traffic. Among the sounds generated by the volcanic activity, impulsive signals have been evidenced and interpreted as proxy for lava flow emplacements. The characteristics and the spatio-temporal evolution of these hydroacoustic signals allowed the estimation of effusion and flow rates, key parameters for volcano monitoring. These sounds are related to the non-explosive quenching of pillow lavas due to the rapid heat transfer between hot lava and cold seawater, with this process releasing an energy equivalent to an airgun source as used for active seismic exploration. Volcano observatories could hence use autonomous hydrophones in the water column to detect and monitor active submarine eruptions in the absence of regular on-site seafloor survey.

Keywords: hydroacoustic monitoring; submarine eruption; Mayotte island

Citation: Lavayssière, A.; Bazin, S.; Royer, J.-Y. Hydroacoustic Monitoring of Mayotte Submarine Volcano during Its Eruptive Phase. *Geosciences* **2024**, *14*, 170. https://doi.org/10.3390/geosciences14060170

Academic Editors: Jesus Martinez-Frias and Karoly Nemeth

Received: 3 May 2024
Revised: 3 June 2024
Accepted: 9 June 2024
Published: 17 June 2024

1. Introduction

Although 75% of the Earth's volcanic activity occurs beneath the oceans' surface [1], ways to detect and monitor it underwater are limited. While aerial volcanoes can be monitored through a vast array of land-based sensors and remote sensing [2–9], underwater volcanic eruption cannot be visually observed and deploying instrumentation can be challenging. Usually, submarine eruptions occur at such water depths that it requires bathymetric surveys and seismo-acoustic methods to detect them and better understand their dynamics. Detected by both hydrophones (in the water column or on the seafloor) and ocean-bottom seismometers (OBS), seismo-acoustic signals give insights into the characteristics, evolution, and dynamics of submarine eruptions in a variety of geodynamical contexts and provide unique observations about otherwise-undetected eruptions [10]. This is due to the exceptional ability of the ocean to propagate acoustic waves.

Sound waves propagate in the ocean at a speed that depends on the salinity, temperature, and pressure of the seawater. These parameters can create a low sound-velocity layer at around 1000 m depth at mid-latitudes, known as the SOund Fixing And Ranging channel (SOFAR) [11,12]. This layer behaves as a waveguide in which low-frequency sounds can propagate with little attenuation over thousands of kilometers [13–15], in contrast with seismic waves that are quickly attenuated in the solid Earth (typically 50–100 km away from an OBS array), e.g., [16].

Analyzing 108 submarine eruptions worldwide,Tepp and Dziak [10] reports that 82% of those are recorded by geophones while 47% are recorded by hydrophones. The

submarine eruption-related processes most commonly detected are earthquakes, similar to aerial volcanoes [17–20]. Earthquakes are detected either by seismic waves reaching the geophones of the OBS arrays, or through their hydroacoustic signals (T-waves), with the seismic waves being converted into acoustic waves at the seafloor and traveling long-distances in the SOFAR channel. However, another process is receiving increasing interest from the scientific community: volcanic explosions, either short [14,21] or sustained [20,22]. Finally, some instrument arrays have been able to detect effusive submarine activity. As they release less acoustic energy, those are much harder to detected [19,23–25]. However, when they are detected, these signals provide information to monitor the timing and location of lava flows and its emplacement rate [24,26]. Those last signals, detected offshore Mayotte island, are the subject of this paper.

Mayotte island, the easternmost island of the Comoros archipelago in the Mozambique Channel, started being shaken by intense seismicity in May 2018 [27,28]. Associated with an important tilt (10–19 cm of subsidence and 21–25 cm eastward displacement) [29,30], this seismicity has been linked with intense magmatic activity at depth, which later gave birth to a new underwater volcanic edifice ~50 km offshore, named Fani Maoré (Figure 1). Comprehensive seismic catalogs [31,32], ground deformation studies [33], and extensive petrological and geochemical analyses [34,35] have helped interpreting the eruption processes of Fani Maoré as well as previous submarine eruptions in the region. Moreover, several lava flows around the new volcanic structure have been evidenced by repeated bathymetric surveys every 6 months to a year. However, all these observations could not reveal the precise chronology of the lava flows.

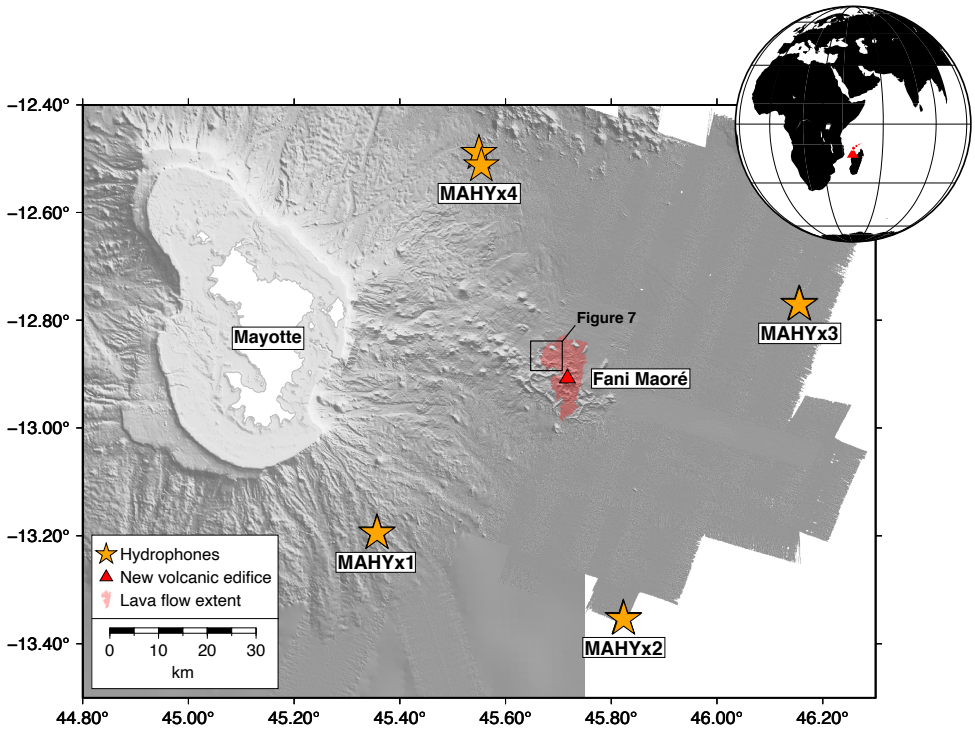

Figure 1. Bathymetric map of the study area showing the location of the new Fani Maoré volcano (red triangle) and its lava flow extent (in red) [29]. Yellow stars are the hydrophone locations of the MAHY network. Inset shows the study area in a global context as a red volcano symbol.

Sounds of lava–water interactions were evidenced by ocean-bottom hydrophones [31] and by the MAHY hydrophone network [36] (Figure 1). Bazin et al. [36] observed numerous impulsive events in the MAHY hydroacoustic data on 15 November 2020. All were consistently located in a recent lava field, mapped by diachronic bathymetric surveys. An on-going flow was even observed in real time by a towed camera showing the red glow of incandescent lavas. From a 10-day deployment of an OBS array in early Octo-

ber 2020, Saurel et al. [31] hand-picked a catalog of hydroacoustic signals related to this fresh lava field from the hydrophone channel of the OBSs. The detected signals were complex to process due to multiple reflections of the acoustic waves on the sea surface and bottom before reaching the OBS at the seafloor. In contrast, signals detected by the moored hydrophones traveled directly from the source to the instruments in the SOFAR channel. These two studies demonstrated that hydroacoustic signals can be used to monitor lava flow emplacements in details, and thus could inform on the eruption effusion rates. Hydroacoustic techniques can hence usefully complement diachronic bathymetric surveys in timing the lava flows.

In the following paper, we present a complete analysis of the impulsive events recorded by the MAHY hydrophone array between mid-October 2020 and July 2022. We focused our analysis on the spatial and temporal distribution of the associated lava flow events. It shows how a hydrophone network can detect and monitor lava flow emplacements in details during a long underwater eruption, and how it could improve our understanding of the dynamics of submarine volcanism worldwide.

2. Materials and Methods

2.1. Hydrophone Deployments and Data

Four autonomous hydrophones (AuHs) have been deployed approximately 50 km away from and surrounding the Fani Maoré volcano (FMV, Figure 1). These four AuHs form the MAHY hydroacoustic network used in this study and in Bazin et al. [36]. The instruments continuously record the soundscape between 2 and 120 Hz and consist of a buoy containing the hydrophone sensor (HTI-90U) and a mooring line anchored to a disposable weight at the seafloor that can be released by an acoustic release (Figure 2). The length of the moorings was set so that all sensors were maintained in the axis of the SOFAR channel, approximately 1300 m below sea level.

The network was first deployed with the instruments MAHY01 to MAHY04 during the MAYOBS15 cruise [37] in October 2020, approximately two years after the start of the seismic activity. It has been maintained three times: in April 2021 (MAYOBS18) [38], in October 2021 (MAYOBS21) [39], and in July 2022 (MAYOBS23) [40]. The moorings were redeployed at nearly the same sites and their number incremented by 10 at every deployment (i.e., MAHY01, MAHY11, MAHY21 for site 1). During MAYOBS21, only three hydrophones were redeployed, as MAHY14 recovery was delayed due to a trigger release problem. The last maintenance was carried out in September 2023 during MAYOBS25 [41], but the corresponding dataset has not been used in this study.

The records are complete for the first 7-month period between October 2020 to April 2021. During the second deployment, between April 2021 and September 2021, MAHY11 recorded 86% of the time, whereas MAHY12, MAHY13, and MAHY14 recorded 77%, 100%, and 96% of the time, respectively. These data gaps were due to battery or SD card failures. In the third deployment, between September 2021 and July 2022, MAHY21 and MAHY23 recorded 100% of the time and MAHY22 stopped recording just one day before its recovery.

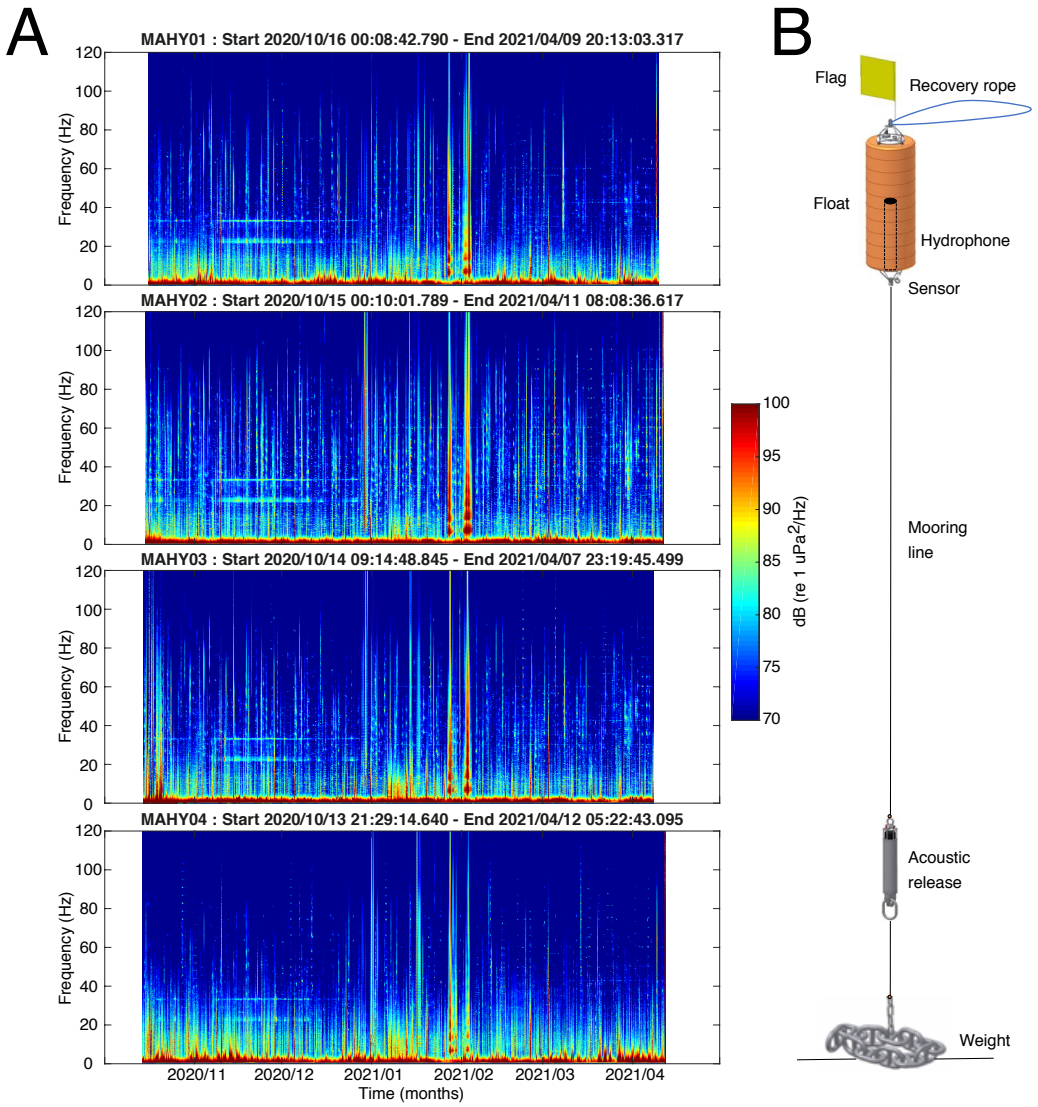

Figure 2. (**A**) Spectrograms of the MAHY data over the first recording period (October 2020–April 2021). Horizontal lines show the presence of whale calls in the southern summer of 2020, while vertical lines mostly reflect marine traffic and seismic surveys (January–February 2021). (**B**) MAHY hydrophone mooring line.

2.2. Manual Picking and Location of Events

Raw data were first corrected for the internal clock drift, which amounts to ∼1–2 s for a 1-year deployment. We then used the Seas software [15] to process the data by simultaneously visualizing 15-min traces and spectrograms from all AuHs. When an event could be identified on at least three hydrophones, we picked their arrival times on each spectrogram and inverted them to locate the source event. The source location and origin time are calculated by a non-linear least-square minimization of the arrival times. The algorithm supposes a direct propagation path between the seafloor sound source and each of the hydrophones and calculates the source coordinates. With four hydrophones, Seas can also estimate uncertainties in latitude, longitude, and origin time. Hence, for our analyses, we only kept events detected by four hydrophones, with estimated uncertainties.

We mainly focused on impulsive events, using the same method as Bazin et al. [36], but we also picked two other types of signals of interest: a few earthquakes and one landslide. We estimated the origin of earthquakes by picking the T-phase arrival times at their maximum amplitude in the spectrograms [25]. In the case of an earthquake, the located source is not the hypocenter but the acoustic radiator on the seafloor (proxy of the

epicenter for a shallow earthquake). We also noticed long signals which we potentially interpreted as submarine landslides. For one of those signals, we picked the first arrival and the maximum of the energy envelope and derived two locations. The picking of the impulsive events was improved in a second iteration by zooming-in on a 120 s time window centered on the event [25].

The Seas software also calculates the source level (SL) of the events in decibels (dB re µPa at 1 m, hereinafter dB), based on the received levels on each hydrophone corrected for the cylindrical and spherical transmission losses between the source and receiver.

3. Results

Our manual screening of the data recorded between October 2020 and July 2022 allowed us to identify different type of events of biological, geological, and man-made origins. In the next section, we present some examples of these acoustic signals.

3.1. Biological and Man-Made Noises

We observed sounds related to marine mammals calls as well as transiting ships (Figure 2). These signals were generally visible on one or two AuHs only and we did not locate their sources. They are the subjects of other studies, e.g., [42].

The hydrophones recorded seismic airgun shots from the SISMAORÉ (27 December 2020 to 4 February 2021) [43] and CARAPASS (20 February 2021 to 7 March 2021) [44] oceanographic cruises (seen as vertical lines on the spectrograms of Figure 2), as well as a non-identified survey in November 2021–January 2022. Seismic shots, 10 to 40 s apart, generate energetic signals of up to 60 Hz that obscure most seismo-acoustic events. We have picked and located a few seismic shots to be used for calibration purposes.

We also noted very short impulsive events that seem to be man-made as they all occurred during daytime (7 a.m. to 4 p.m. local time). Most of these events were seen on only three AuHs and hence could not be properly located. The arrival times and the fact that they are best detected by MAHY4 (NW site) suggest that their most likely sources are blasts from two quarries in the coastal areas of Koungou and Kangani in NE Mayotte.

3.2. T Phases of Earthquakes

Many earthquakes were recorded by the MAHY network. When an earthquake occurs, seismic waves convert into acoustic energy at the seafloor [45,46] that will then propagate with minimal attenuation, and hence over large distances, across the SOFAR channel. The resulting T-waves generally have a recognizable waveform in the hydroacoustic data and MAHY's events do not differ (Figure 3). Due to the limited extent of the network and to the proximity of the earthquakes, P and S seismic waves arrivals are often easily discernible in the acoustic data. These early arrivals correspond to P and S waves converting into acoustic waves at the foot of the mooring. Their occurrence is rare on wider networks, and/or for distant sources, because the seismic energy vanishes before reaching the AuHs.

We attempted to locate some large earthquakes from T-wave arrivals in our dataset, but their location was 5 to 78 km (in average 18 km) away from their actual epicenters in seismic catalogs [47]. Given that the Mayotte seismic activity is uncommonly deep (25–50 km below seafloor), it illustrates that, in such a case, the seismo-acoustic conversion area on the seafloor is not always the epicenter. This discrepancy, likely due to seismic heterogeneities in the upper lithosphere (i.e., complex seismic ray paths), would be worth investigating but is beyond the scope of this paper.

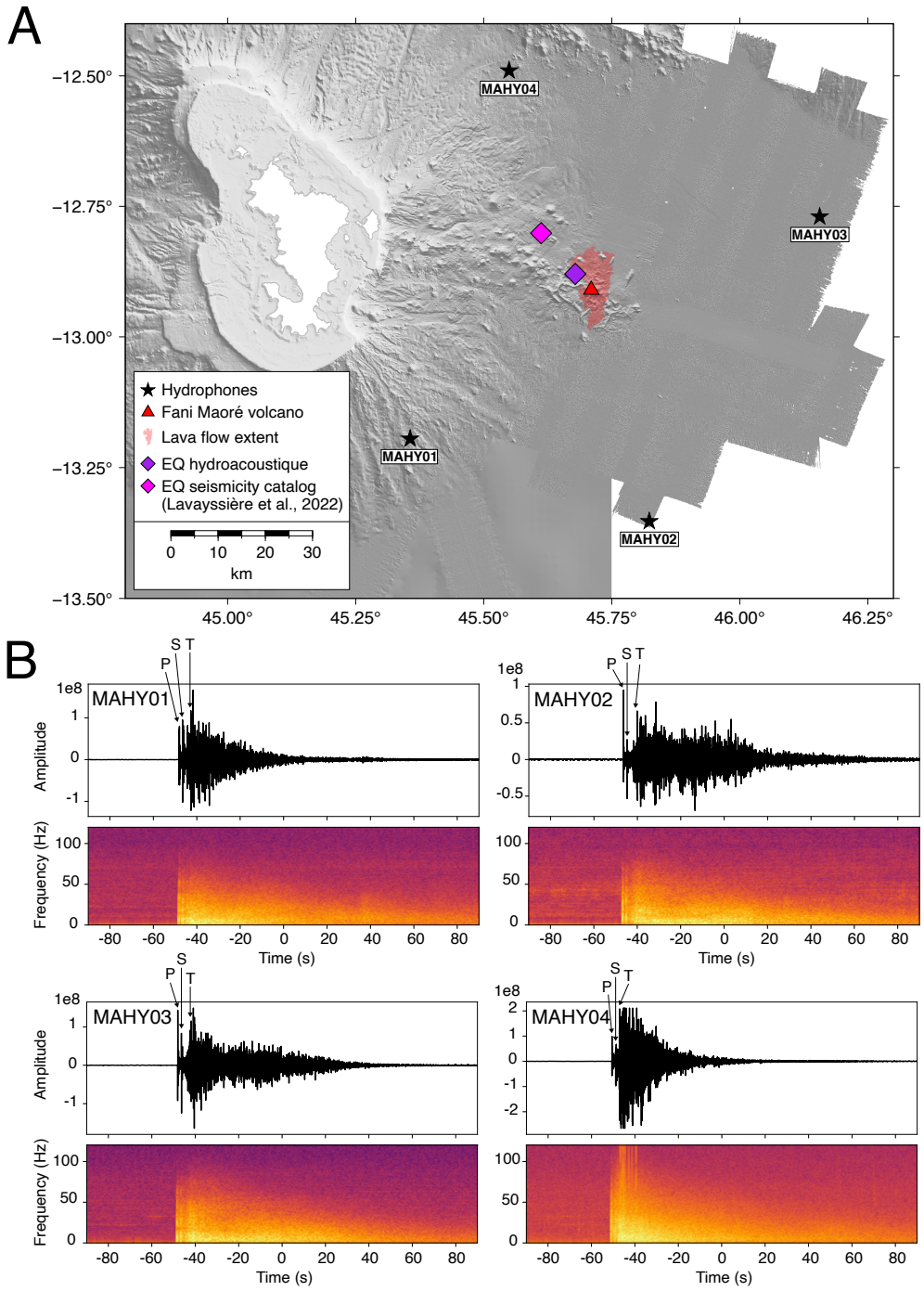

Figure 3. Location map and records of an earthquake that occurred on 22 November 2020. (**A**) Earthquake locations from the trilateration of AuH data (purple diamond) and from OBS data (pink diamond). See interpretation and discussion in the text. (**B**) Three-minute-long hydroacoustic signals and spectrograms for the four hydrophones. The P-, S-, and T-phase arrivals of the earthquake are clearly recognizable.

3.3. Submarine Landslides

We noticed a potential submarine landslide on the 25 October 2020, at 04:26. We estimated two locations from our two picking methods (Figure 4). The 1st arrivals yielded a location at the top of a ridge, with errors of 1.5 km, 1.8 km, and 0.8 s in latitude, longitude, and origin time, respectively (Figure 4A). The envelop maxima yielded a down-slope location, with errors of 2 km, 2.5 km, and 1.1 s in latitude, longitude, and origin time,

respectively (Figure 4A). The fact that the second location is at the bottom of a slope compared to the first location strengthens the hypothesis of a submarine landslide.

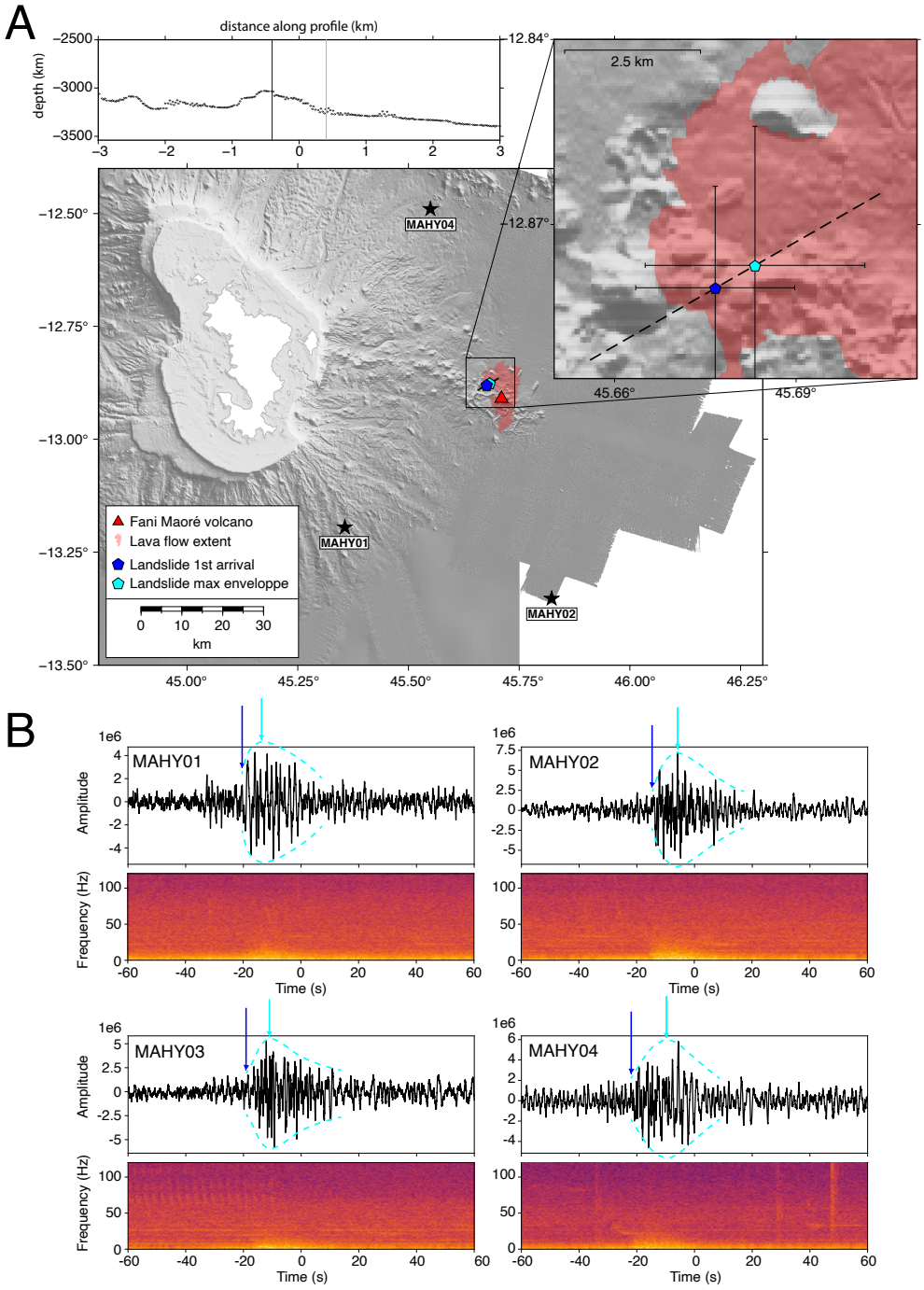

Figure 4. Possible landslide event on 25 October 2020 at 04:27. (**A**) Map and cross-section: blue star in map and blue line in profile show the location based on first T-phase arrivals while the cyan ones show the location derived from maximum energy arrivals. (**B**) Two-minute-long signals and spectrograms of this event recorded by the four hydrophones. The picked arrival times are indicated with the same color code than in (**A**).

3.4. Impulsive Events

Our visual analysis of the data between 16 October 2020 and 13 July 2022 leads to a catalog of 584 impulsive lava events, all jointly recorded by the four MAHY hydrophones. These signals are very energetic (in average 190 dB with minimum 182 and maximum

203 dB), up to 120 Hz, and very short (<5 s) (Figure 5A). Such characteristics indicate that these waves are water-born (H-waves), meaning that they are generated directly in the water and not from a seismo-acoustic conversion. The two-step picking procedure reduced by ∼2-fold the latitude, longitude, and origin time uncertainties, which are now in the order of 270 m, 340 m, and 0.14 s, respectively (Figure 5B).

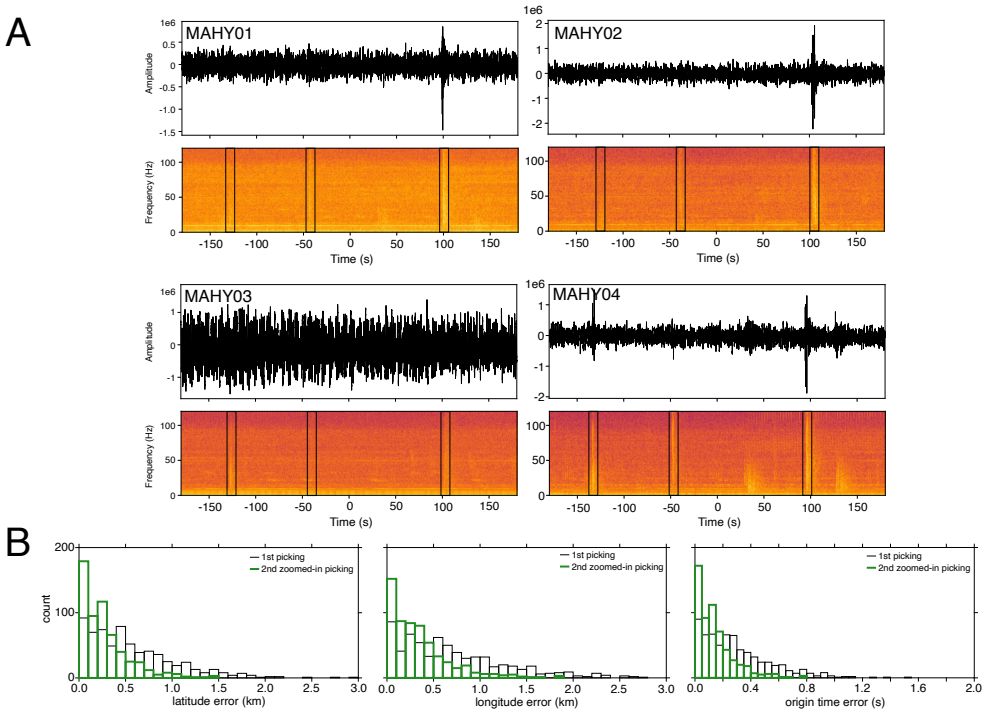

Figure 5. (**A**) Six-minute-long raw waveforms and spectrograms of three impulsive events that occurred on 6 November 2020 (black boxes). Note that one of these events is visible in the time signal of 3 out of 4 hydrophones, whereas the two others are only visible in the spectrograms. (**B**) Histograms of the errors in latitude, longitude, and origin time for the catalog of 584 impulsive events after the first (black) and after the second (green) iteration of the picking process.

The events occurred only in the first three months of our recording period, in swarms of 4 to 7 days, and stopped after 4 December 2020 (Figure 6). To ensure that no event was missed because they were not detected on at least three hydrophones, we scanned the data hydrophone by hydrophone and found no such event after 4 December 2020.

The events are all located in the same active lava field, known as the Tiktak region (Figure 7), as observed in previous studies [31,36]. They slightly shifted in location over time: the later events (dark purple dots) are mainly clustered on a topographic high to the southeast of the Tiktak lava field while all other events are clustered inside the Tiktak field, but with a slight shift to the northeast with time. In the following discussion, we analyze in more details the spatial and temporal distribution of those lava events.

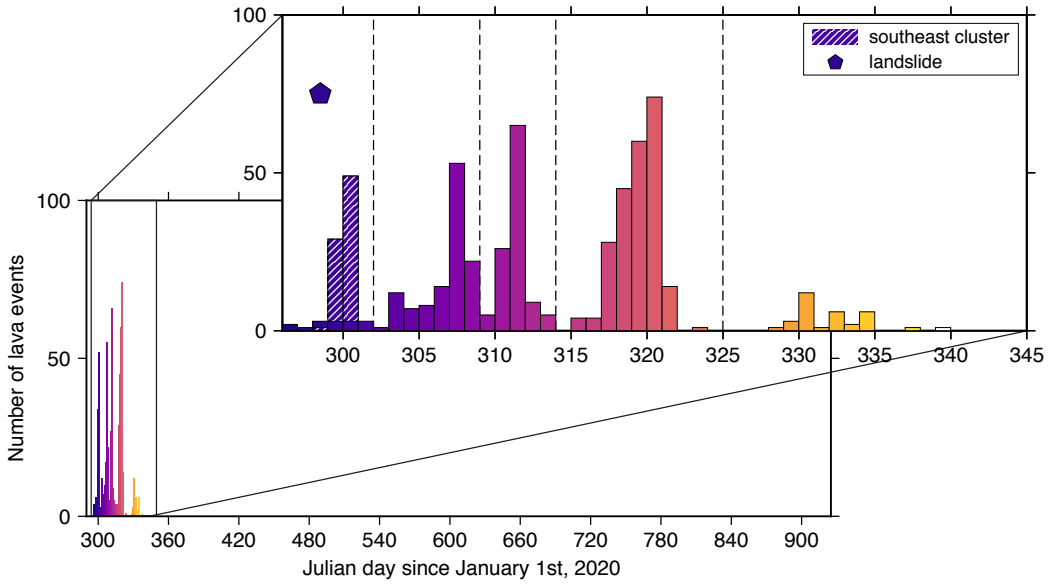

Figure 6. Chronogram of impulsive events from the beginning of the hydroacoustic monitoring in October 2020 until July 2022. Colors represent time. Note the early southeast cluster events highlighted by stippled lines. The possible landslide of 25 October 2020 is indicated as a hexagon color-coded by time. See interpretation in the text.

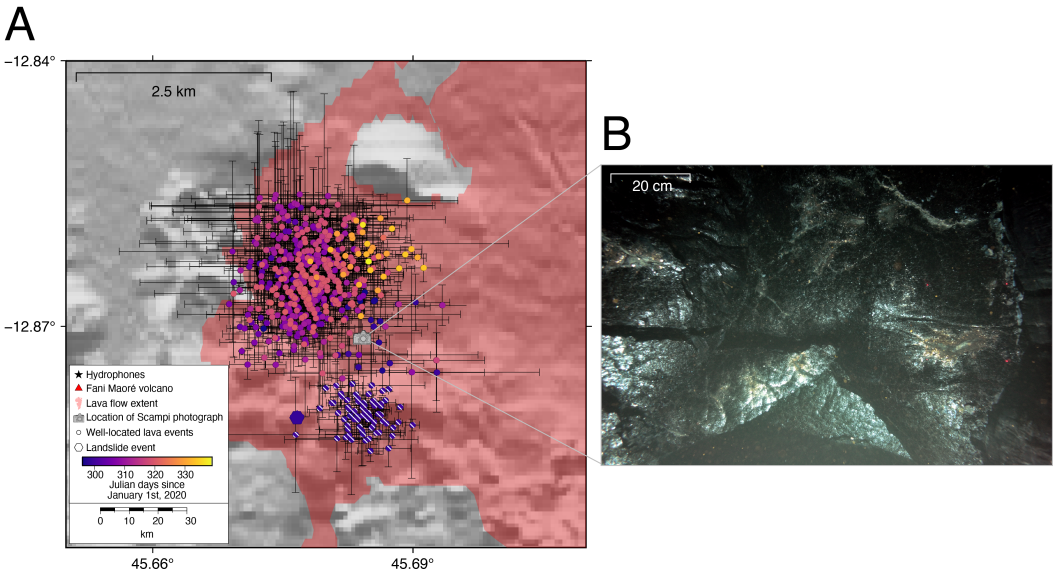

Figure 7. (**A**) Evolution of the lava flow/impulsive events in the zoomed area shown in Figure 1. Events are color-coded by time of occurrence in the Tiktak area (same color scale as in Figure 6). Note the location of the possible landslide (purple hexagon) and of the underwater photography (gray camera symbol) presented in (**B**). (**B**) Photograph taken during the Scampi dive number 135 on 20 October 2020 at 06:02 (MAYOBS15 cruise) [37]. Note the fresh lava flow associated with small <5-cm wide cracks and the absence of fragmented, explosive-like pieces.

4. The Eruptive Phase of Fani Maoré: Processes Inferred from Hydroacoustic Data

Two active lava flow zones were observed during the network monitoring period (Figure 7). They are concentrated in time over the first 3 months of recording, likely pinpointing the exact time of the final eruptive phase of the eruption: 4 December 2020. This hydroacoustic study was the only one able to pinpoint this exact date. Further details can be inferred on the eruptive processes of Fani Maoré submarine activity between October and December 2020.

4.1. Evolution in Space and Time of the Lava Flows

The lava flows in the Tiktak area form a relatively circular shape of ~2.5 km diameter. Based on successive ship-borne multibeam bathymetric surveys, the average lava thickness, produced from October 2020 to January 2021, is no more than 10 m in the south of the Tiktak [36]. It is the threshold of detection for the echosounder and suggests that the rest of the Tiktak lava flows is probably thinner. Approximating the Tiktak area to a cylinder with a diameter of 2.5 km and a height of 10 m, the volume of newly erupted lava would be in the order of $\sim 49.10^6$ m^3. If we now consider that the impulsive events date the emplacement of the lava and that they occurred in the 41 days between the first and last swarms, the effusion rate can be estimated to 14 m^3/s. Using continuous GNSS data, Peltier et al. [33] had estimated the effusion rate by modeling the observed surface deformation and the associated volume variation over time. They computed that the source flow rate decreased from 357 $\pm$ 60 m^3/s in December 2018 to 5 $\pm$ 7 m^3/s in 2021. Thus, our instantaneous rate estimate falls within the expected range. For comparison, at Axial Seamount, along the Juan de Fuca Ridge, Gregg and Fink [48] determined an effusion rate of ~100 m^3/s, based on laboratory simulations and seafloor observations of lava flow morphology. For the same submarine volcano, Le Saout et al. [24] estimated an average extrusion rate of 22–45 m^3/s during the 2015 eruption, by timing impulsive lava events with ocean-bottom hydrophones over a 28-day period. Thus, although lower, our estimate of effusion rate for the Fani Maoré eruption is in the order of magnitude of published values. Moreover, as it correlates with the end of the lava flow activity, it seems fair to suggest a lower effusion rate than at a more intense phase of eruptive activity.

The lava flow signals are distributed within two main swarms, hereafter called the northern and southern swarms. They were most likely generated by two distinct volcanic vents. The southern vent was probably not active at the very beginning of our monitoring period. One event on the morning of 24 October 2020 preceded the southern swarm that occurred on 25 and 26 October 2020 (Julian calendar days 299 to 300). During this time, the northern vent was active but at low intensity over 6 days (less than five events/day between Julian calendar days 296 and 301, Figure 6). The activity of the southern vent, located on a bathymetric high, coincides in space and time with the presumed landslide of 25 October 2020 (Figures 4, 6 and 7). The landslide occurred at 04:27 on the 25th and, except for the one event on the 24th, the southern swarm started just after, at 04:42. We suggest that lava accumulation at the edge of the ridge provoked an instability and triggered the landslide. However, there is not enough information to relate the landslide with the start of the hydroacoustic cluster. Observations of submarine landslide are rare in the literature but Lee et al. [49] estimated the velocity of a sediment landslide in 1929 (from breakage of submarine telephone cables) up to 28 m/s. If we consider the downward distance (~800 m) and the duration of the observed landslide signal (~30 s) (Figure 4), we can estimate a maximum velocity of 26 m/s for our submarine landslide.

After this small swarm in the Southeast, lava flowed only within the lower and flat part of the Tiktak area (Figure 7) in swarms separated by one to several days of low or no activity (Figure 6). The last swarm, in yellow in Figures 6 and 7, is less intense, with only a few events per day before the activity completely stopped on 4 December 2020. Between the last two swarms, there is a small relative shift to the Northeast with time. Assuming a migration of the activity of ~1 km between the center of the fourth swarm (pink circles) and the center of the last and fifth swarm (yellow circles), in 14 days—from Julian calendar day 319 to Julian calendar day 333 (middle dates of both swarms)—we can infer an insignificant migration of the last lava flows at 0.0008 m/s, about 13-fold less than observed during the 2015 Axial seamount eruption [24] and probably representative of the end of the eruptive phase.

4.2. Mechanism Causing the Lava Events

Impulsive lava flow events have already been observed at several submarine volcanoes, e.g., [14,20,50–53] and are generally thought to be due to hot lava reaching the seafloor

and interacting with the cold seawater. However, how such interaction generates sounds is not yet understood and hypotheses range from the sudden breaking of part of the solid lava crust (quenching) to gas bubble bursting. A rapid heat transfer when lava and seawater are in contact can lead to both explosive fragmentation of magma and non-explosive quenching [54]. Both types of mechanisms were observed during offshore lava emplacements at Kilauea in 2018 [55] and generated impulsive hydroacoustic events similar to ours, although at a much shallower depth than this study.

Fresh lava flows were observed and filmed in situ with a deep-tow camera survey on 20 October 2020 along a transect that crossed the entire Tiktak area (MAYOBS15) [37]. The video showed glowing red lava in a cracked pillow [36]. In the region of the northern swarm, the video showed fresh morphologies of almost exclusively pillow lavas with relatively small cracks (Figure 7B). No signs of lava fragmentation due to submarine explosions were observed. Thus, for the Fani Maoré eruption, we favor the non-explosive quenching of pillow lava due to the rapid heat transfer between hot lava and cold seawater as the origin of the impulsive events.

4.3. Energy Released by Lava Events

The MAHY network recorded many airgun shots from the SISMAORÉ seismic survey [43] (Figure 8). Thanks to information on the shot source location and size, we can compare the sound intensity of the impulsive events (in dB) with the energy released by airguns.

The SISMAORÉ exploration survey used two airgun sources of different volumes—S1 at 300 cubic inches and S2 at 2570 cubic inches—shot at different intervals, 10 and 40 s, respectively, and at 140 bar (2030 psi) [56]. For each type of sources, we picked five shots located near the center of the AuH array and close to the lava flow events for a better comparison, and compared their expected source levels with those calculated with Seas (Figure 8).

The source S1 is expected to generate a peak sound level of 234.5 dB at a reference distance of 1 m compared to the average SL of 191 dB computed from our hydroacoustic records. The stronger source S2 emitted a peak sound level of 251.2 dB at a reference distance of 1 m while Seas estimated a source level of 206 dB. As our lava events have an average SL of ∼190 dB, we interpret that their source releases an energy equivalent to a 300 cubic-inch source similar to the array used for S1.

The ∼45 dB difference between the expected peak sound level of the airgun shots and our estimated SL of the airgun shots is likely due to Seas integrating the receiver level of the hydroacoustic signals over a 10 s time window. Indeed, the Sound Exposure Level (SEL), which integrates the signal over 5 s, provides an expected level of only 208 dB for S1 and 229 dB for S2 [56], thus reducing the observed sound level discrepancy to ∼20 dB. We suggest that this difference is due to the 10 s integration window of Seas processing software.

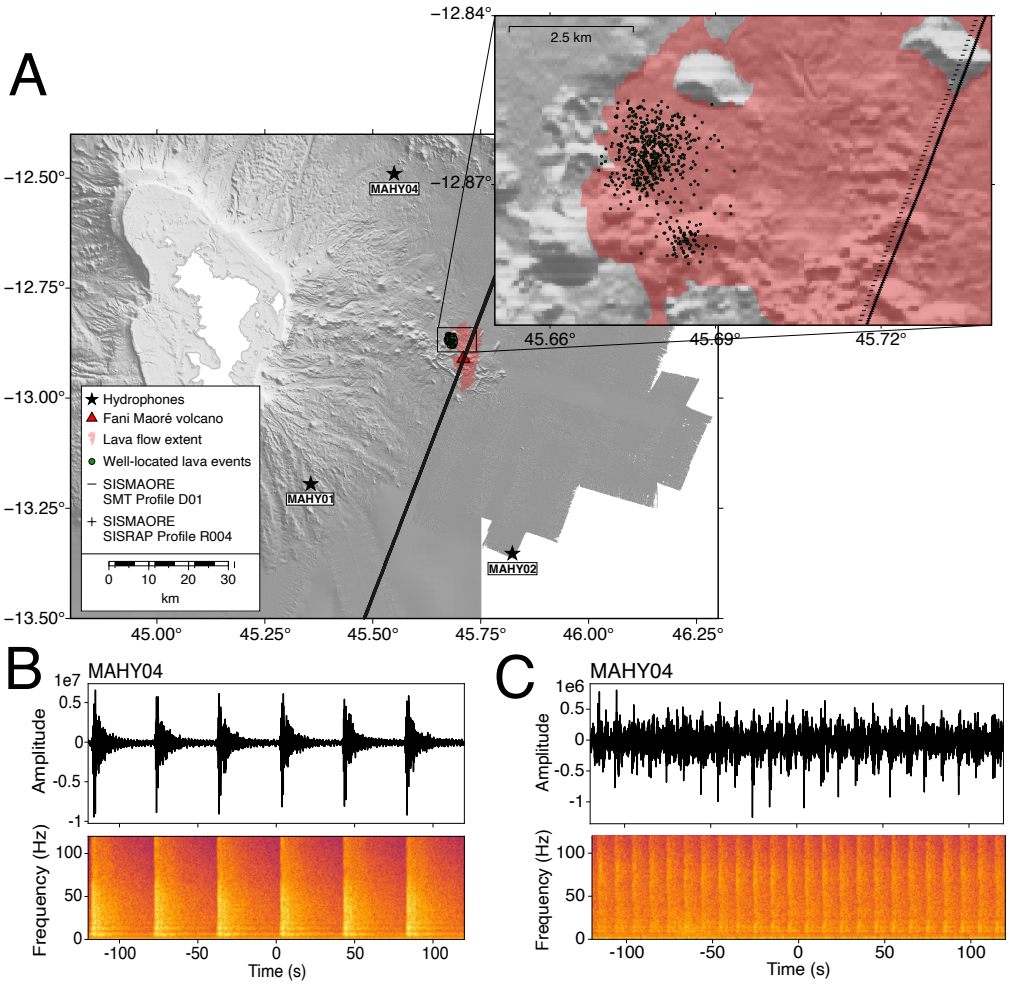

Figure 8. (**A**) Location map of seismic airgun shots. Blacks lines represent a traces of the shots. Inset is a closer view of these locations. (**B**) Four−minute−long hydroacoustic signals and spectrograms for one AuH (MAHY04).

5. Conclusions

The Fani Maoré eruption offshore Mayotte in the western Indian Ocean provided a new opportunity to investigate a submarine volcanic eruption with four autonomous hydrophones deployed 50 km away from the new volcanic edifice. In addition to a large variety of sounds recorded between October 2020 and July 2022, nearly 600 impulsive hydroacoustic events were detected, located, and interpreted as a proxy for lava flow emplacements. This activity occurred in the first three months of monitoring, from October to December 2020. The lack of events since then suggests that the eruptive activity ended on the 4 December 2020.

The lava events occurred in irregular swarms during 41 days, separated by non-uniform periods of low to no activity. They are focused over a limited area of ∼4.9 km^2, known as the Tiktak lava field. Combining this information with the estimated volume of lava produced during this period yielded an effusion rate of 14 m^3/s, lesser than active volcanoes on mid-ocean ridges such as at the Axial Seamount, but representative of the ending of the eruptive phase of the Fani Maoré volcano. Thus, hydroacoustic monitoring can usefully complement diachronous bathymetric surveys to estimate key eruption parameters without visual observations.

Although this analysis is only a small snapshot of the Fani Maoré eruption that lasted nearly 2 years, it shows that (autonomous) hydrophones are very efficient tools to detect, locate, and time lava flow emplacements and perhaps, in the future, new volcanic bursts of this volcano.

Author Contributions: Conceptualization, A.L. and S.B.; formal analysis, A.L. and S.B.; investigation, A.L.; methodology, S.B.; resources, S.B. and J.-Y.R.; supervision, S.B.; writing—original draft and figures, A.L.; writing—review and editing, A.L., S.B. and J.-Y.R. All authors have read and agreed to the published version of the manuscript.

Funding: Since June 2019, all monitoring activities performed on Mayotte by the REVOSIMA (https://doi.org/10.18715/mayotte.revosima) are funded by MESRI (Higher Education, Research and Innovation Ministry), MTE (Environment Ministry) and MOM (Overseas Territory Ministry) with the support from MI (Interior Ministry), MINARM (Armed Forces Ministry), and DIRMOM (joint-government department for Major Hazards in the Overseas). A.L. was financially supported by DEAL (Environment Department) Mayotte and the Department of Finistère.

Data Availability Statement: The MAHY data contribute to the Specific Action Sismologie Marine Mobile of Epos-France (www.epos-france.fr/en/). A catalog of the impulsive events discussed in this paper is available at the SEANOE data repository (https://doi.org/10.17882/100655).

Acknowledgments: All marine operations were part of the MAYOBS series of cruises conducted on the R/V Marion Dufresne and R/V Pourquoi Pas ? (https://doi.org/10.18142/291) and we thank their captains and crews. GMT [57] and ObsPy [58] were used to create the figures and Nikon NX Studio (https://www.nikon.fr/fr_FR/product/apps-software/nx-studio) was used to post-process the Scampi photograph. We express our gratitude to Mickael Beauverger and Jonathan Tanrin for their technical support at Geo-Ocean, and to Benoit Loubrieu for his help with the Scampi photographs.

Conflicts of Interest: The authors declare no conflicts of interest.

Abbreviations

The following abbreviations are used in this manuscript:

AuHs	Autonomous Hydrophones
SOFAR	SOund Fixing And Ranging
OBSs	Ocean Bottom Seismometers
FMV	Fani Maoré Volcano
RL	Receiver Level
SEL	Sound Exposure Level
SL	Source Level

References

1. Crisp, J.A. Rates of magma emplacement and volcanic output. *J. Volcanol. Geotherm. Res.* **1984**, *20*, 177–211. [CrossRef]
2. Inguaggiato, S.; Mazot, A.; Ohba, T. Monitoring active volcanoes: The geochemical approach. *Ann. Geophys.* **2011**, *54*, 115–119. [CrossRef]
3. Biasi, J.; Tivey, M.; Fluegel, B. Volcano Monitoring with Magnetic Measurements: A Simulation of Eruptions at Axial Seamount, Kīlauea, Bárðarbunga, and Mount Saint Helens. *Geophys. Res. Lett.* **2022**, *49*, e2022GL100006. [CrossRef]
4. De Plaen, R.S.M.; Lecocq, T.; Caudron, C.; Ferrazzini, V.; Francis, O. Single-station monitoring of volcanoes using seismic ambient noise. *Geophys. Res. Lett.* **2016**, *43*, 8511–8518. [CrossRef]
5. Schiavo, B.; Stremme, W.; Grutter, M.; Campion, R.; Guarin, C.A.; Rivera, C.; Inguaggiato, S. Characterization of a UV camera system for SO_2 measurements from Popocatépetl Volcano. *J. Volcanol. Geotherm. Res.* **2019**, *370*, 82–94. [CrossRef]
6. Stremme, W.; Grutter, M.; Baylón, J.; Taquet, N.; Bezanilla, A.; Plaza-Medina, E.; Schiavo, B.; Rivera, C.; Blumenstock, T.; Hase, F. Direct solar FTIR measurements of CO_2 and HCl in the plume of Popocatépetl Volcano, Mexico. *Front. Earth Sci.* **2023**, *11*, 1022976. [CrossRef]
7. McNutt, S.R.; Roman, D.C. Chapter 59-Volcanic Seismicity. In *The Encyclopedia of Volcanoes*, 2nd ed.; Academic Press: Amsterdam, The Netherlands, 2015; pp. 1011–1034. [CrossRef]
8. Power, J.A.; Haney, M.M.; Botnick, S.M.; Dixon, J.P.; Fee, D.; Kaufman, A.M.; Ketner, D.M.; Lyons, J.J.; Parker, T.; Paskievitch, J.F.; et al. Goals and Development of the Alaska Volcano Observatory Seismic Network and Application to Forecasting and Detecting Volcanic Eruptions. *Seismol. Res. Lett.* **2020**, *91*, 647–659. [CrossRef]
9. Peltier, A.; Bachèlery, P.; Staudacher, T. Magma transport and storage at Piton de La Fournaise (La Réunion) between 1972 and 2007: A review of geophysical and geochemical data. *J. Volcanol. Geotherm. Res.* **2009**, *184*, 93–108. [CrossRef]
10. Tepp, G.; Dziak, R.P. The Seismo-Acoustics of Submarine Volcanic Eruptions. *J. Geophys. Res. Solid Earth* **2021**, *126*, e2020JB020912. [CrossRef]
11. Swainson, O.W. Velocity and ray paths of sound waves in sea water. *US Coast Geod. Surv. Field Eng. Bull* **1936**, *10*, 64.

12. Ewing, M.; Woollard, G.P.; Vine, A.C.; Worzel, J.L. Recent results in submarine geophysics. *Geol. Soc. Am. Bull.* **1946**, *57*, 909–934. [CrossRef]
13. Dziak, R.P.; Fox, C.G. Evidence of harmonic tremor from a submarine volcano detected across the Pacific Ocean basin. *J. Geophys. Res. Solid Earth* **2002**, *107*, ESE 1-1–ESE 1-11. [CrossRef]
14. Tepp, G.; Chadwick, W.W.; Haney, M.M.; Lyons, J.J.; Dziak, R.P.; Merle, S.G.; Butterfield, D.A.; Young, C.W. Hydroacoustic, Seismic, and Bathymetric Observations of the 2014 Submarine Eruption at Ahyi Seamount, Mariana Arc. *Geochem. Geophys. Geosystems* **2019**, *20*, 3608–3627. [CrossRef]
15. Fox, C.G.; Matsumoto, H.; Lau, T.A. Monitoring Pacific Ocean seismicity from an autonomous hydrophone array. *J. Geophys. Res. Solid Earth* **2001**, *106*, 4183–4206. [CrossRef]
16. Schmid, F.; Schlindwein, V. Microearthquake activity, lithospheric structure, and deformation modes at an amagmatic ultraslow spreading Southwest Indian Ridge segment. *Geochem. Geophys. Geosystems* **2016**, *17*, 2905–2921. [CrossRef]
17. Matoza, R.S.; Okubo, P.G.; Shearer, P.M. Comprehensive High-Precision Relocation of Seismicity on the Island of Hawai'i 1986–2018. *Earth Space Sci.* **2021**, *8*, 1–10. [CrossRef]
18. Jurado, M.J.; Ripepe, M.; Lopez, C.; Ricciardi, A.; Blanco, M.J.; Lacanna, G. Underwater records of submarine volcanic activity: El Hierro (Canary Islands 2011–2012) eruption. *J. Volcanol. Geotherm. Res.* **2020**, *408*, 107097. [CrossRef]
19. Wilcock, W.S.D.; Tolstoy, M.; Waldhauser, F.; Garcia, C.; Tan, Y.J.; Bohnenstiehl, D.R.; Caplan-Auerbach, J.; Dziak, R.P.; Arnulf, A.F.; Mann, M.E. Seismic constraints on caldera dynamics from the 2015 Axial Seamount eruption. *Science* **2016**, *354*, 1395–1399. [CrossRef] [PubMed]
20. Tepp, G.; Dziak, R.P.; Haney, M.M.; Lyons, J.J.; Searcy, C.; Matsumoto, H.; Haxel, J. Seismic and hydroacoustic observations of the 2016–17 Bogoslof eruption. *Bull. Volcanol.* **2020**, *82*, 4. [CrossRef]
21. Matsumoto, H.; Zampolli, M.; Haralabus, G.; Stanley, J.; Mattila, J.; Meral Özel, N. Interpretation of detections of volcanic activity at Ioto Island obtained from in situ seismometers and remote hydrophones of the International Monitoring System. *Sci. Rep.* **2019**, *9*, 19519. [CrossRef]
22. Wright, I.C.; Chadwick, W.W.; de Ronde, C.E.J.; Reymond, D.; Hyvernaud, O.; Gennerich, H.; Stoffers, P.; Mackay, K.; Dunkin, M.A.; Bannister, S.C. Collapse and reconstruction of Monowai submarine volcano, Kermadec arc, 1998–2004. *J. Geophys. Res. Solid Earth* **2008**, *113*. [CrossRef]
23. Caplan-Auerbach, J.; Dziak, R.P.; Haxel, J.; Bohnenstiehl, D.R.; Garcia, C. Explosive processes during the 2015 eruption of Axial Seamount, as recorded by seafloor hydrophones. *Geochem. Geophys. Geosystems* **2017**, *18*, 1761–1774. [CrossRef]
24. Le Saout, M.; Bohnenstiehl, D.R.; Paduan, J.B.; Clague, D.A. Quantification of Eruption Dynamics on the North Rift at Axial Seamount, Juan de Fuca Ridge. *Geochem. Geophys. Geosystems* **2020**, *21*, e2020GC009136. [CrossRef]
25. Ingale, V.V.; Bazin, S.; Olive, J.; Briais, A.; Royer, J.Y. Hydroacoustic Study of a Seismic Swarm in 2016–2017 near the Melville Transform Fault on the Southwest Indian Ridge. *Bull. Seismol. Soc. Am.* **2023**, *113*, 1523–1541. [CrossRef]
26. Tan, Y.J.; Tolstoy, M.; Waldhauser, F.; Wilcock, W.S.D. Dynamics of a seafloor-spreading episode at the East Pacific Rise. *Nature* **2016**, *540*, 261–265. [CrossRef]
27. Feuillet, N.; Jorry, S.; Crawford, W.C.; Deplus, C.; Thinon, I.; Jacques, E.; Saurel, J.M.; Lemoine, A.; Paquet, F.; Satriano, C.; et al. Birth of a large volcanic edifice offshore Mayotte via lithosphere-scale dyke intrusion. *Nat. Geosci.* **2021**, *14*, 787–795. [CrossRef]
28. Lemoine, A.; Briole, P.; Bertil, D.; Roullé, A.; Foumelis, M.; Thinon, I.; Raucoules, D.; de Michele, M.; Valty, P.; Hoste Colomer, R. The 2018–2019 seismo-volcanic crisis east of Mayotte, Comoros islands: Seismicity and ground deformation markers of an exceptional submarine eruption. *Geophys. J. Int.* **2020**, *223*, 22–44. [CrossRef]
29. REVOSIMA. Bulletin Mensuel. Technical Report, 2024. Available online: https://www.ipgp.fr/actualites-du-revosima/ (accessed on 23 March 2024).
30. Briole, P. Note sur la crise tellurique en cours à Mayotte. Technical Report, 2018. Available online: http://volcano.iterre.fr/wp-content/uploads/2018/11/mayotte_note_deformation_GPS_20181126.pdf (accessed on 23 March 2024).
31. Saurel, J.M.; Retailleau, L.; Deplus, C.; Loubrieu, B.; Pierre, D.; Frangieh, M.; Khelifi, N.; Bonnet, R.; Ferrazzini, V.; Bazin, S.; et al. Combining hydro-acoustic sources and bathymetric differences to track the vent evolution of the Mayotte eruption, Mozambique Channel. *Front. Earth Sci.* **2022**, *10*, 983051. [CrossRef]
32. Lavayssière, A.; Retailleau, L. Capturing Mayotte's deep magmatic plumbing system and its spatiotemporal evolution with volcano-tectonic seismicity. *Volcanica* **2023**, *6*, 331–344. [CrossRef]
33. Peltier, A.; Saur, S.; Ballu, V.; Beauducel, F.; Briole, P.; Chanard, K.; Dausse, D.; De Chabalier, J.B.; Grandin, R.; Rouffiac, P.; et al. Ground deformation monitoring of the eruption offshore Mayotte. *Comptes Rendus. Géosci.* **2023**, *354*, 171–193. [CrossRef]
34. Berthod, C.; Médard, E.; Bachèlery, P.; Gurioli, L.; Di Muro, A.; Peltier, A.; Komorowski, J.C.; Benbakkar, M.; Devidal, J.L.; Langlade, J.; et al. The 2018-ongoing Mayotte submarine eruption: Magma migration imaged by petrological monitoring. *Earth Planet. Sci. Lett.* **2021**, *571*, 117085. [CrossRef]
35. Verdurme, P.; Gurioli, L.; Chevrel, O.; Médard, E.; Berthod, C.; Komorowski, J.C.; Harris, A.; Paquet, F.; Cathalot, C.; Feuillet, N.; et al. Magma ascent and lava flow field emplacement during the 2018–2021 Fani Maoré deep-submarine eruption insights from lava vesicle textures. *Earth Planet. Sci. Lett.* **2024**, *636*, 118720. [CrossRef]
36. Bazin, S.; Royer, J.Y.; Dubost, F.; Paquet, F.; Loubrieu, B.; Lavayssière, A.; Deplus, C.; Feuillet, N.; Jacques, E.; Rinnert, E.; et al. Initial results from a hydroacoustic network to monitor submarine lava flows near Mayotte Island. *Comptes Rendus. Géosci.* **2023**, *354*, 257–273. [CrossRef]

37. Rinnert, E.; Thinon, I.; Feuillet, N. Oceanographic Campaign MAYOBS15. 2020. [CrossRef]
38. Rinnert, E.; Thinon, I.; Lebas, E. Oceanographic Campaign MAYOBS21. 2021. [CrossRef]
39. Rinnert, E.; Thinon, I.; Lebas, E. Oceanographic Campaign MAYOBS18. 2021. [CrossRef]
40. Jorry, S.; Paquet, F.; Lebas, E. Oceanographic Campaign MAYOBS23. 2022. [CrossRef]
41. Thinon, I.; Lebas, E. Oceanographic Campaign MAYOBS25. 2023. [CrossRef]
42. Dréo, R. Étude de la saisonnalité des grandes baleines à l ' est de Mayotte (Océan Indien) à partir de données Rapport d ' étude. Technical Report, 2023.
43. Thinon, I.; Leroy, S.; Lemoine, A. Oceanographic Campaign SISMAORÉ. 2020. [CrossRef]
44. Division Plans de DMI-SHOM. Oceanographic Campaign CARAPASS 2021. 2021. Available online: https://campagnes.flotteoceanographique.fr/campaign (accessed on 23 March 2024).
45. Tolstoy, I.; Ewing, M. The T phase of shallow-focus earthquakes*. *Bull. Seismol. Soc. Am.* **1950**, *40*, 25–51. [CrossRef]
46. Talandier, J.; Okal, E.A. On the mechanism of conversion of seismic waves to and from T waves in the vicinity of island shores. *Bull. Seismol. Soc. Am.* **1998**, *88*, 621–632. [CrossRef]
47. Lavayssière, A.; Crawford, W.C.; Saurel, J.M.; Satriano, C.; Feuillet, N.; Jacques, E.; Komorowski, J.C. A new 1D velocity model and absolute locations image the Mayotte seismo-volcanic region. *J. Volcanol. Geotherm. Res.* **2022**, *421*, 107440. [CrossRef]
48. Gregg, T.K.P.; Fink, J.H. Quantification of submarine lava-flow morphology through analog experiments. *Geology* **1995**, *23*, 73. [CrossRef]
49. Lee, H.J.; Locat, J.; Desgagnés, P.; Parsons, J.D.; McAdoo, B.G.; Orange, D.L.; Puig, P.; Wong, F.L.; Dartnell, P.; Boulanger, E. Submarine mass movements on continental margins. In *Continental Margin Sedimentation: From Sediment Transport to Sequence Stratigraphy*; Jarvis, I., Nittrouer, C.A., Austin, J.A., Field, M.E., Kravitz, J.H., Syvitski, J.P.M., Wiberg, P.L., Eds.; Blackwell Publishing: Malden, MA, USA, 2007; Volume 37, pp. 213–274. [CrossRef]
50. Chadwick, W.W.; Cashman, K.V.; Embley, R.W.; Matsumoto, H.; Dziak, R.P.; de Ronde, C.E.J.; Lau, T.K.; Deardorff, N.D.; Merle, S.G. Direct video and hydrophone observations of submarine explosive eruptions at NW Rota-1 volcano, Mariana arc. *J. Geophys. Res. Solid Earth* **2008**, *113*, *B08S10*. [CrossRef]
51. Green, D.N.; Evers, L.G.; Fee, D.; Matoza, R.S.; Snellen, M.; Smets, P.; Simons, D. Hydroacoustic, infrasonic and seismic monitoring of the submarine eruptive activity and sub-aerial plume generation at South Sarigan, May 2010. *J. Volcanol. Geotherm. Res.* **2013**, *257*, 31–43. [CrossRef]
52. Dziak, R.P.; Bohnenstiehl, D.R.; Baker, E.T.; Matsumoto, H.; Caplan-Auerbach, J.; Embley, R.W.; Merle, S.G.; Walker, S.L.; Lau, T.; Chadwick, W.W. Long-term explosive degassing and debris flow activity at West Mata submarine volcano. *Geophys. Res. Lett.* **2015**, *42*, 1480–1487. [CrossRef]
53. Crone, T.J.; Bohnenstiehl, D.R. Acoustic evidence of a long-lived gas-driven submarine volcanic eruption in the Bismarck Sea. *Geophys. J. Int.* **2019**, *217*, 169–178. [CrossRef]
54. Murch, A.P.; Portner, R.A.; Rubin, K.H.; Clague, D.A. Deep-subaqueous implosive volcanism at West Mata seamount, Tonga. *Earth Planet. Sci. Lett.* **2022**, *578*, 117328. [CrossRef]
55. Costa, O. Investigating Kīlauea's 2018 Offshore Lava Emplacement through Hydroacoustic Data. Ph.D. Thesis, Western Washington University, Washington, DC, USA, 2023.
56. Ducatel, C. Campagne SISMAORE N/O Pourquoi Pas? Analyse des Risques Sonores Potentiels. Technical Report, IFREMER, 2020. Available online: https://archimer.ifremer.fr (accessed on 23 March 2024).
57. Wessel, P.; Luis, J.F.; Uieda, L.; Scharroo, R.; Wobbe, F.; Smith, W.H.F.; Tian, D. The Generic Mapping Tools Version 6. *Geochem. Geophys. Geosystems* **2019**, *20*, 5556–5564. [CrossRef]
58. Beyreuther, M.; Barsch, R.; Krischer, L.; Megies, T.; Behr, Y.; Wassermann, J. ObsPy: A Python Toolbox for Seismology. *Seismol. Res. Lett.* **2010**, *81*, 530–533. [CrossRef]